Experimental Mechanics (2011) 51:591–607
DOI 10.1007/s11340-011-9463-6

In-situ AFM Experiments with Discontinuous DIC Applied to Damage Identification in Biomaterials

D. Grégoire · O. Loh · A. Juster · H.D. Espinosa

Received: 30 July 2010 / Accepted: 3 January 2011 / Published online: 12 February 2011

Abstract Natural materials (e.g. nacre, bone, and spider silk) exhibit unique and outstanding mechanical properties. This performance is due to highly evolved hierarchical designs. Building a comprehensive understanding of the multi-scale mechanisms that enable this performance represents a critical step toward realizing strong and tough bio-inspired materials. This paper details a multi-scale experimental investigation into the toughening mechanisms in natural nacre. By applying extended digital image correlation and other image processing techniques, *quantitative* information is extracted from otherwise prodominantly *qualitative* experiments. *In situ* three point bending fracture tests are performed to identify and quantify the toughening mechanisms involved during the fracture of natural nacre across multiple length scales. At the macro and micro scales, fracture tests performed *in situ* with a macro lens and optical microscope enable observation of spreading of damage outward from the crack tip. This spreading is quantified using an iso-contour technique to assess material toughness. At the nanoscale, fracture tests are performed *in situ* an atomic force microscope to link the larger-scale damage spreading to sliding within the tablet-based microstructure. To quantify the magnitude of sliding and its distribution, images from the *in situ* AFM fracture tests are analyzed using new algorithms based on digital image correlation techniques which allow for discontinuous displacement fields. Ultimately, this comprehensive methodology provides a framework for broad experimental investigations into the failure mechanisms of bio- and bio-inspired materials.

Keywords Natural nacre · Nanocomposite · Fracture and damage · Multiscale *in situ* experiments · Atomic force microscopy · Digital image correlation · Image processing

Introduction

Many materials found in nature are comprised of relatively weak materials, yet they still exhibit superior mechanical performance. This performance originates within elegant hierarchical structures (e.g., bone, nacre, wood, spider silk [1–5]). Nacre from Abalone shells, also known as Mother-of-Pearl, exhibits remarkable strength and toughness despite its composition of greater than 95% aragonite, a brittle ceramic [6, 7]. By incorporating just 5% soft biopolymer into a hierarchical structure with the brittle ceramic, nacre is ~1000 times tougher than pure aragonite [8, 9]. This significant increase in toughness stems from toughening mechanisms that act at multiple length scales within the hierarchical structure. At the macroscale, growth lines towards the inner part of the shell help deflect propagating cracks and serve as a last source of protection for the Abalone [10, 11]. However, nacre's micro- and nano-scale architecture is a more significant contributor to this increase in toughness. At the micro-scale, aragonite ceramic tablets and thin biopolymer layers form a brick-and-mortar-like structure [12, 13]. Under

D. Grégoire · O. Loh (SEM member) · A. Juster (SEM member) ·
H.D. Espinosa (✉, SEM fellow)
Department of Mechanical Engineering, Northwestern University,
2145 Sheridan Road,
Evanston, IL 60208, USA
e-mail: espinosa@northwestern.edu

Present Address:
D. Grégoire
Laboratoire des Fluides Complexes et leurs Reservoirs,
Université de Pau et des Pays de l'Adour,
Allée du Parc Montaury,
64600 Anglet, France

loading, these tablets slide relative to each other. Espinosa, et al. proposed that microscale waviness in the surface of these tablets generates transverse compressive stresses as they slide, resulting in a progressive hardening of the interface [2, 14]. This interfacial hardening is believed to be a primary mechanism for the spreading of damage over large areas (large crack process zone), resulting in the extraordinary toughness of nacre. At the nanoscale, several toughening mechanisms have also been identified that act at the sliding interface between tablets. These include nanoscale asperities on the surface of the tablets that increase friction or interlocking during relative sliding [15], mineral bridges between tablets [16–22], and unfolding of proteins in the biopolymer "mortar" layer [23].

In this manuscript, we detail a comprehensive experimental approach to investigate the tablet sliding-based toughening mechanisms of natural nacre. This approach combines *in situ* fracture tests using optical and atomic force microscopy (AFM) to characterize damage spreading at multiple scales with image processing and discontinuous digital image correlation algorithms to quantify these results. We begin with sample preparation techniques and a discussion of the macro- and micro-scale *in situ* fracture tests. At this scale, characteristics such as material toughness are assessed. However, these experiments also highlight the need for quantitative nanoscale investigations to explain the underlying fundamental mechanisms that are active within the observed fracture process zone. Thus we progress to nanoscale fracture tests *in situ* the AFM to observe the material response at the single tablet level. To quantify the tablet sliding observed in the *in situ* AFM fracture tests, we apply digital image correlation techniques.

Because of nacre's brick-and-mortar structure, the displacement fields become discontinuous at the interfaces between tablets as they slide. This detrimentally affects the outcome of conventional DIC techniques [24]. Here we demonstrate a discontinuous DIC method capable of capturing and quantifying the discontinuous sliding at the interface between ceramic tablets in nacre. Given this technique, we can precisely quantify and observe material behavior in areas that would conventionally fall outside the scope of traditional DIC. Thus the experimental methods and analyses presented herein are also more broadly applicable to discontinuous composites or biomaterials, as well as nacre-inspired materials such as those designed through large scale layered composites [25, 26], layer-by-layer deposition [27–29], thin film deposition [30], self assembly [31], and ice templation [32].

Material and Methods

Sample Preparation

Notched samples were prepared for three point bending fracture tests according to the ASTM Standard E1820 [33] normalized Single-Edge Notched Beam (SENB) design. The steps involved in the sample preparation are performed under hydrated conditions as follows:

- the raw shell [Fig. 1(a)] is cut with a conventional diamond saw into rectangular pieces of 50×50 mm size;
- the top calcite layer is removed and the nacre exposed using a grinding wheel (180 grit paper);
- strips of nacre are cut using a high precision rotary saw (Accutom 5) fitted with a diamond blade (Ukam 330CA);
- the faces of the nacre strips are rectified with a conventional grinder;
- the final SENB shape and pre-notch are obtained using the Accutom saw fitted with a jewelry diamond blade (Primecut–Crystalite corp). The microstructure of the pre-notched samples is shown in Fig. 1(b).

The resulting SENB sample geometry is shown in Fig. 2. The specimens are cut and notched such that the crack

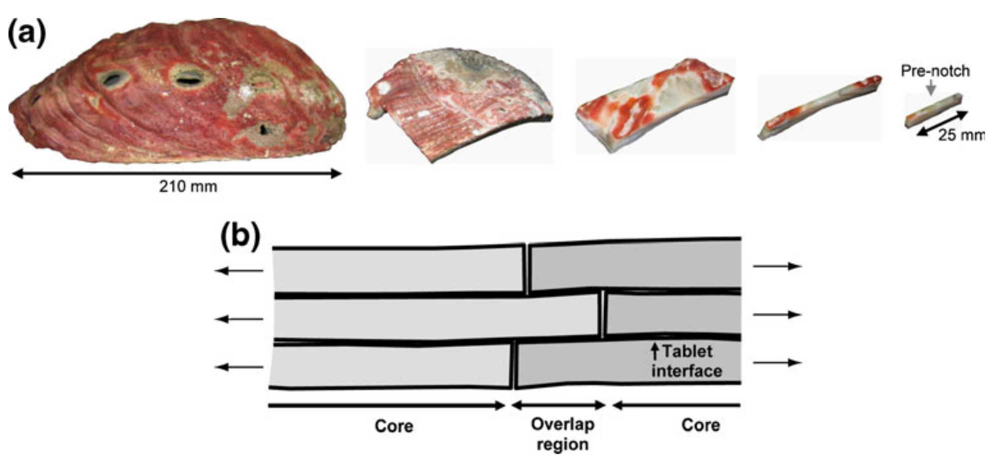

Fig. 1 (**a**) Sample preparation from red abalone shell. (**b**) Schematic of typical microstructure showing overlapping tablet arrangement and direction of loading/tablet sliding

Fig. 2 Single-Edge Notched Beam (SENB) sample geometry

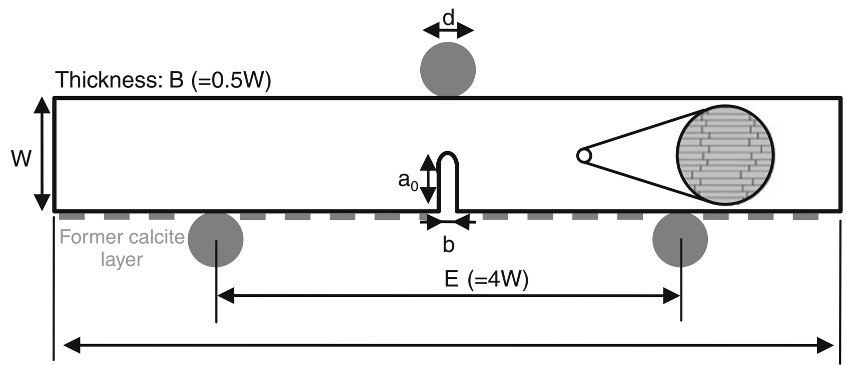

would propagate perpendicularly to the tablet layers, beginning from the calcite layer side and moving toward the animal.

Description of Test Rig and Experimental Procedure

The testing rig consists of a three-point bending fixture mounted on a miniature loading stage (Ernest Fullam, Inc). The imposed displacement is measured by a linear variable differential transformer (LVDT – HS50/13053) and accompanying acquisition electronics (Newport Inc, INF-B model). The resulting force is measured by a 100-lb load cell (Honeywell Sensotec, model 31) and accompanying acquisition electronics (Honeywell Sensotec, model SC500). Both signals are recorded and synchronized through a Matlab script.

Depending on the scale of interest, the test rig was integrated with different imaging tools: macro-lens (ML), optical microscope (OM), or atomic force microscope (AFM) to observe, *in-situ*, the deformation mechanisms at different scales.

Within this manuscript, four fracture tests performed at different scales on natural nacre samples carved from two different raw shells (labeled A and B in Fig. 3) are presented and analyzed. The purpose of the various tests is to identify and quantify the mechanisms involved during the fracture of natural nacre from the macroscale to the nanoscale. The two shells, obtained from the same abalone species, are similar in shape and size but are different in color. We purposely investigated two very different shells to assess the generality of the observed phenomena. Moreover, large shells were acquired (~210 mm in length) to be able to manufacture suitable fracture specimens. The resulting sample geometries are summarized in Table 1.

Damage and Fracture Mechanisms at the Macroscale

In situ fracture test #1 (Table 1) was performed under a classical macroscale optical apparatus (camera and macro-lens) in order to observe evolution of the fracture process during crack propagation in natural nacre. Figure 4 shows

Fig. 3 Different abalone shells investigated in this study

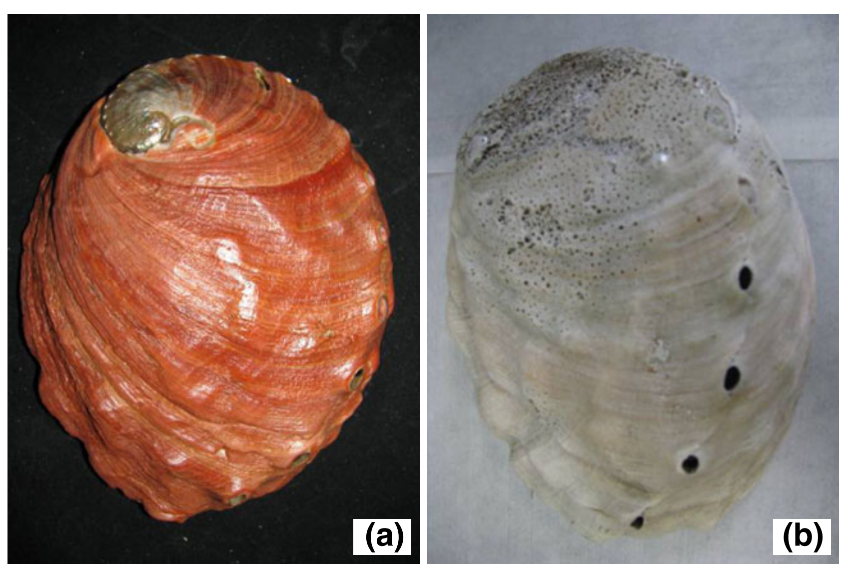

Table 1 Dimensions and observation modes for the tested samples

Test	Observation mode	Raw shell (Fig. 3)	Dimensions (mm) (Fig. 2)						
			L	W	B	d	E	a_0	b
#1	Macro-lens	A	25.05	3.69	1.73	1.58	14.4	1.74	0.66
#2	Optical microscope	B	25.01	3.55	1.73	1.58	14.4	1.80	0.66
#3	AFM	A	25.06	3.64	1.75	1.58	14.4	1.87	0.66
#4	AFM	B	24.97	3.61	1.62	1.58	14.4	1.76	0.66

the crack propagation history and Fig. 5 presents the corresponding load-deflection profile. As the load increases, a region of whitish appearance emerges from the notch tip (becomes clearly visible at t=35 s in Fig. 4). This zone, linked to the damage spreading process, grows up to the onset of cracking at approximately t=41 s. It then propagates ahead of the notch tip generating a well-defined damage process zone. For instance, at t=47 s, the white region is 250 μm ahead of the notch tip. Finally at t=51 s, the crack reaches the growth lines and deflects along them.

Figure 5 shows a typical load-deflection profile exhibiting an initial loading phase followed by a sudden drop in load associated to crack growth. When the crack reaches the network of growth lines, it branches to follow a complex path through them. The sample thus sustains additional loading before complete failure as illustrated by the load-deflection curve. It is worth noting that crack deflection along the growth lines serves as a final barrier against catastrophic failure in the samples tested. However, the unique fracture properties of nacre are instead linked to the tablet-based damage spreading phenomenon which acts throughout the initial crack propagation, rather than this growth line mechanism which is active only very late in the fracture process. Thus, in order to better characterize the evolution of the spreading zone during crack propagation, additional experiments were designed and performed at smaller scales.

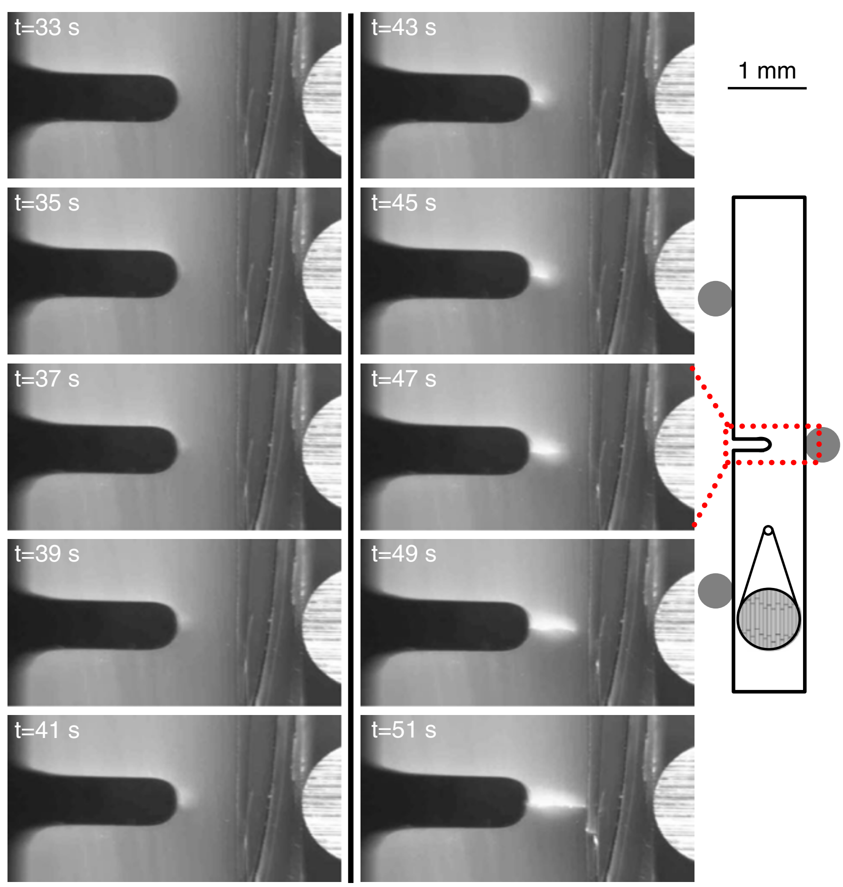

Fig. 4 Crack propagation history for fracture test #1

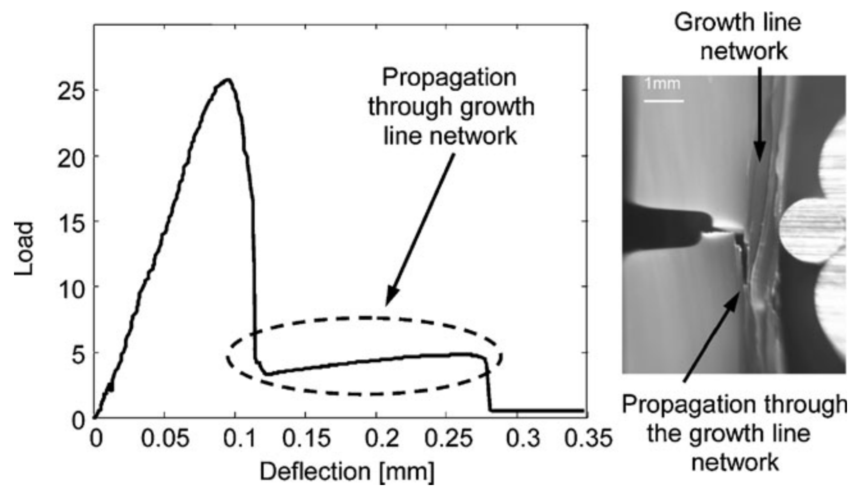

Fig. 5 Load versus deflection profile history for test #1 and crack propagation through the growth lines network

Damage and Fracture Mechanisms at the Microscale

The second *in situ* fracture test (test #2) was performed under an optical microscope to better quantify the fracture process and the corresponding damage spreading during crack propagation in natural nacre (Fig. 6, see also Appendix A). During the test, load-deflection data was recorded continuously [Fig. 6(a)], along with optical images through the microscope [Fig. 6(d)]. The crack length was measured from these images, allowing con-

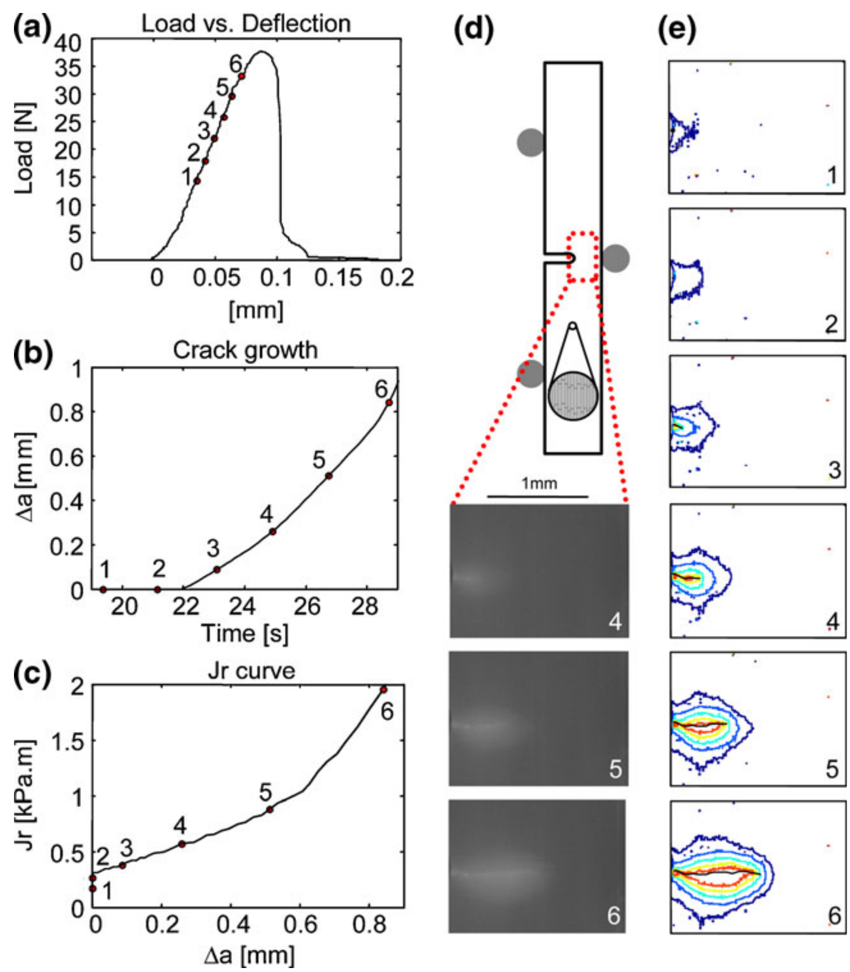

Fig. 6 *In situ* fracture test #2: (**a**) load-deflection curve as measured from the three-point bending apparatus; (**b**) crack growth history; (**c**) Jr-Δa crack resistance curve obtained following the ASTM Standard E1820 (33); (**d**) damage spreading history (raw pictures); (**e**) damage spreading history (processed pictures)

struction of the crack propagation history [Fig. 6(b)]. The corresponding Jr-Δa crack resistance curve was then computed [Fig. 6(c)] following the ASTM Standard E1820 [33]. Details of the procedure to compute the Jr-Δa curve are presented in [9]. In each plot [Fig. 6(a–c)], specific instances within the propagation history are highlighted with a number. The corresponding raw pictures of the crack propagation are presented in Fig. 6 (d). In Fig. 6(e), these raw images have been processed to show the evolution of damage by plotting contours of constant grey level intensity. When natural nacre is damaged, gaps open between the ends of the tablets as they slide relative to each other. By illuminating the nacre sample from the top, light scatters inside the openings, creating a whitish appearance in the damaged region. The greater the degree of damage, tablet sliding, the greater the light scattering. From each raw image, contours of constant grey level intensity (which are thus representative of damage level) are processed using Matlab and the damage spreading history is obtained by keeping the grey level scale constant in the sequence of acquired images.

Figure 6 also provides key information about the damage and fracture mechanisms in natural nacre at the microscale. Considering the load-deflection curve and the corresponding images together reveals that crack initiation occurs before peak load. It further shows that the load continues to increase during crack propagation. Looking at the crack propagation history [Fig. 6(b)], we see that the crack propagation is stable during the first millimeter of the crack growth. This fracture behavior of nacre is further described by examination of Fig. 6(c), which shows an increase in the Jr-Δa curve. Here the Jr value is characteristic of the energy required for the crack to propagate. By the end of the propagation, Jr has increased to approximately 2 kPa.m (starting from ~0.3 kPa.m at crack initiation). Hence, the required energy to fracture the material is 6.6 times higher than its value at initiation, and 200 times higher than the energy required for a crack to propagate in pure aragonite (Jr<0.01 kPa.m [9]). This means that cracks (or defects in general) require more energy to propagate within the material and justifies the excellent crack arrest capabilities and fracture resistance of natural nacre compared to its individual constituents. As described above, Fig. 6(d) shows the spreading of damage during development of the white region (typical of interfacial openings between the tablets), while Fig. 6 (e) shows the same images after processing to indicate the degree of damage spreading. The material starts to damage before crack initiation. Following the iso-contours through the series of images, we see that the damaged region evolves always ahead of the crack tip at about a constant longitudinal velocity. Moreover, the longitudinal expansion velocity of the damage (~0.1 mm/s) is 3.3 times higher than the radial expansion velocity (~0.03 mm/s).

Postmortem SEM Observation

To further characterize the mechanisms behind the white region genesis, postmortem observations were made by scanning electron microscopy on the sample from fracture test #2. Following the fracture test, samples were imaged in an FEI Nova NanoSEM scanning electron microscope. To avoid static charging of these electrically insulating samples, imaging was conducted using a Helix low-vacuum detector at a chamber pressure of 90 mTorr of water vapor (the water vapor atmosphere acts to conduct charge away from the sample).

Figure 7 shows the microstructure in a region encompassing the free crack surface as imaged by SEM. Damage (tablet sliding) is noticeable at the interface between tablets. As expected, the magnitude of tablet sliding decreases slightly with increasing distance from the crack surface. Damage is primarily located at tablet interfaces where neighboring tablets have slid relative to each other, with very few broken tablets observed. These images support the premise that fracture and damage mechanisms in natural nacre are linked to tablet sliding. The fact that the tablet sliding is widely spread around the crack is consistent with the diffusion of the white region, produced by light scattering inside gaps that open between tablets as they slide as observed in Fig. 6.

To accurately quantify this tablet sliding, additional *in-situ* fracture tests were needed at higher magnification. To avoid drying the soft organic layer between tablets which has been shown to influence the mechanical behavior of natural nacre, fracture tests should be performed under hydrated conditions [9]. Therefore, atomic force microscopy was selected over the scanning electron microscopy described above as it required operation in vacuum which would quickly dry the sample.

Preliminary *In Situ* AFM Experiment

In situ fracture test #3 was performed under an atomic force microscope in order to qualify and observe the extent of tablet sliding with sub-nanometer resolution. Notched samples were tested in three-point bending *in situ* the AFM. The Fullam tensile testing machine configured for three-point bending tests was mounted in a Veeco Instruments DI 3100 AFM. This enabled simultaneous loading and imaging of the samples. To avoid imaging artifacts due to thermal drift, the testing machine was mounted in the AFM at least 12 h prior to each test. This allowed all components to reach thermal equilibrium. To further reduce

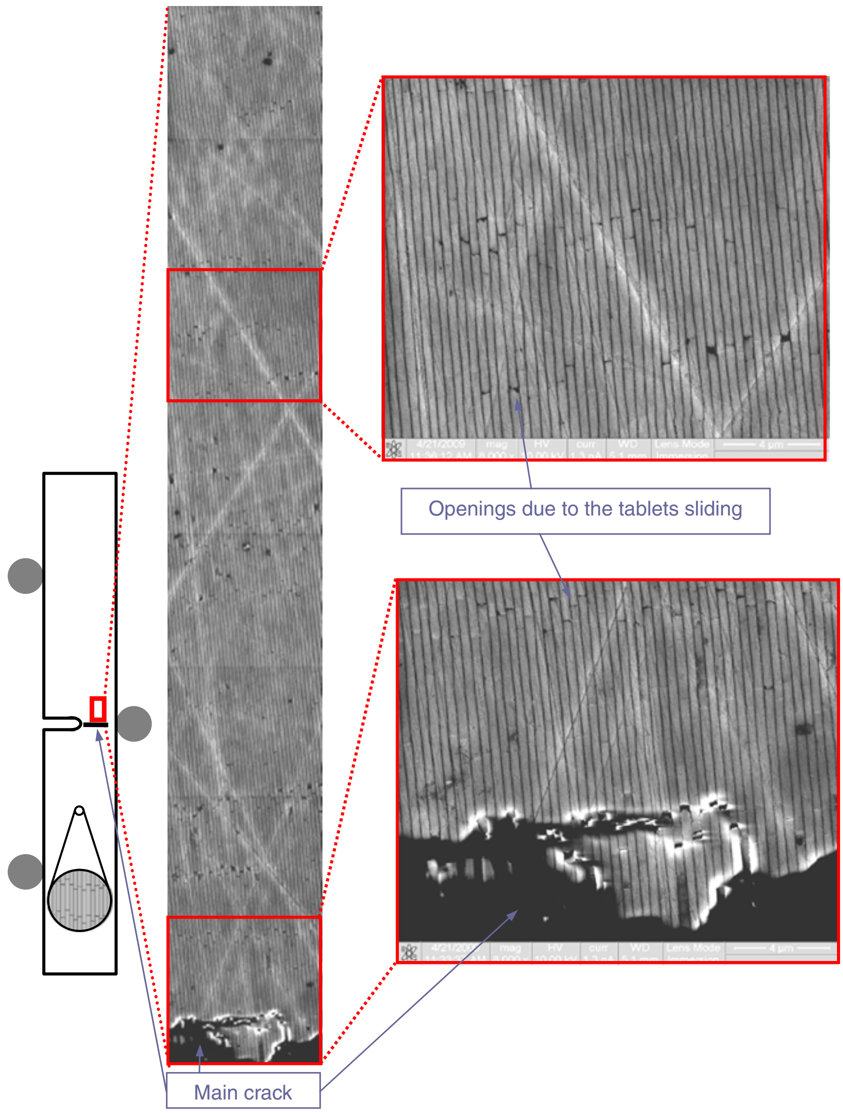

Fig. 7 Postmortem observations of openings by means of scanning electron microscopy

drift, the AFM and Fullam system were turned on at least one hour prior to each test.

Each *in situ* test consisted of repeated incremental loading and AFM imaging. Before the first loading step, reference images of the region of interest were captured using the AFM in tapping mode. The sample was then incrementally loaded in steps while the region of interest was scanned between each loading step. This process was repeated until failure of the sample. This enabled capturing of tablet sliding throughout the loading and crack propagation process.

During each AFM scan, two signals are acquired simultaneously then converted into images. One corresponds to the topography of the sample surface, while the other corresponds to the amplitude of the corresponding error signal. While the topography signal has a more direct physical meaning and is thus used for the following quantitative analysis, the error signal allows more clear visualization of the individual tablets and the opening gaps between them in some cases.

Figure 8 depicts the loading history of fracture test #3 and a representative subset of the corresponding AFM images. In total, four loading steps are separated by three phases of AFM scanning. During the loading phases, the material deforms and tablets slide relative to each other. An elastic energy is stored during this tablet sliding. During imaging, the loading was temporarily paused (displacement held constant with displacement-controlled loading). The stored elastic energy is partially released during this period as the tablets rearrange. This phenomenon, which results in a partial relaxation in the measured load during imaging, could not be avoided since the loading must be paused temporarily to allow for stable *in situ* AFM imaging.

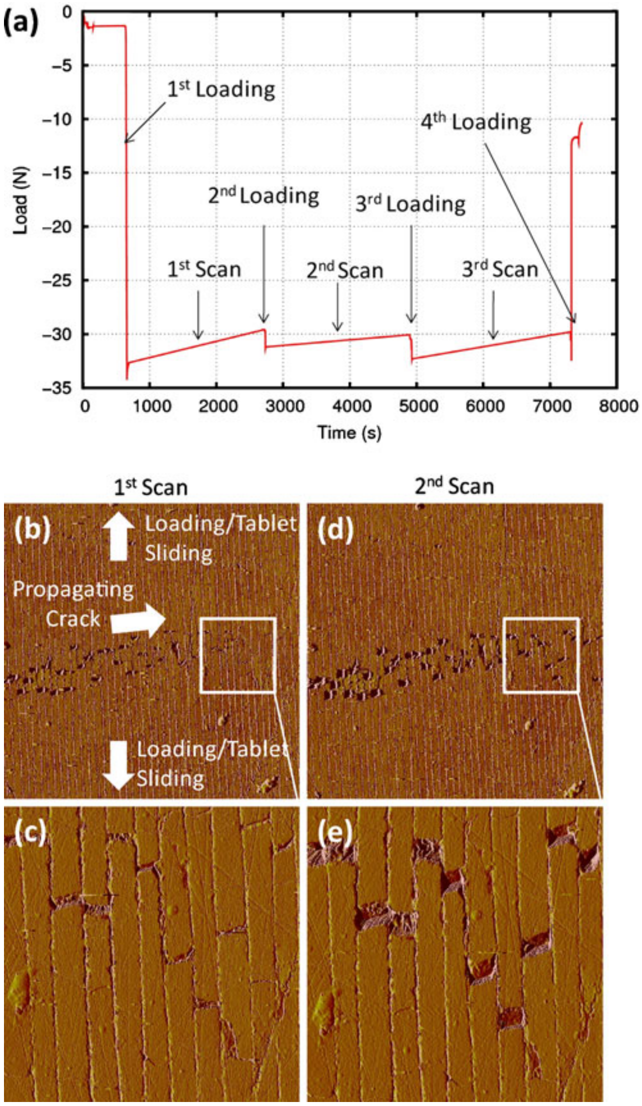

Fig. 8 Results of preliminary *in situ* AFM fracture test (test #3). (**a**) Load history recorded during the test. Load was applied in 4 stages, with AFM imaging conducted between each state. (**b**–**e**) AFM images (error signal amplitude) captured after the first (**b**,**c**) and second (**d**,**e**) loading steps

Figure 8(b, c) shows a set of AFM images obtained during the first scan [conducted after the first loading, Fig. 8(a)]. A row of large openings at the ends of tablets, associated with the path of the primary crack, has just entered the field of view [Fig. 8(b)]. This crack path is not continuous however, but instead composed of several short openings at tablet interfaces where no actual crack tip can be located. This confirms that crack propagation is achieved by tablet sliding in a process zone. It further indicates that non-linear fracture mechanics theory [9] is needed to quantify crack resistance in such a material. Due to the large size of the fracture process zone, the small-scale yielding approximation is not valid for nacre, and stress field analysis, concepts of stress intensity factors, or path independent integrals are in a sense ambiguous when no crack tip or crack lips can be localized. At the macroscale, this tablet arrangement leads to large deformations and hardenings of the whole nacre structure.

Clearly, damage occurs primarily at the interfaces between tablets (tablets sliding relative to each other), although some imperfections are also observed. A mean interface opening of 90 nm is measured from Fig. 8(c), along with a mean tablet length and width of 7.4 µm and 0.45 µm, respectively. A mean organic layer thickness of 25 nm is also measured (shell A). As reported in previous studies [34], the surfaces of the tablets are somewhat wavy rather than being perfectly flat as is apparent from the variations in tablet thickness along their length.

Figure 8(d, e) shows the same region as in Fig. 8(b, c), but after the second loading [Fig. 8(a)]. At this more advanced loading stage, the process zone has grown such that its most advanced edge is now beyond the field of view (i.e., significant tablet sliding is observed across the entire image). The mean interface opening is now 320 nm.

This preliminary test (test #3) confirmed the feasibility of using *in-situ* AFM fracture tests to capture damage propagation at the single tablet level, and provided rough quantitative measurements of tablet sliding. Next, more detailed *in situ* AFM fracture tests are combined with digital image correlation to provide a more robust quantitative analysis of tablet sliding during fracture.

Damage and Fracture Mechanisms at the Nanoscale: Quantification of Tablet Sliding Through an Extended AFM Image Correlation Technique

In Situ AFM Fracture Test (test #4)

Fracture test #4 was performed *in situ* the AFM with the goal of using digital image correlation to process the corresponding images and quantify the extent of tablet sliding at different loads. In general, digital image correlation algorithms require at least two images: one which serves as a reference (e.g., at zero load), and another in a deformed (e.g., loaded) state. In test #4, different positions (P_1, P_2 and P_3) were scanned repeatedly as the load was increased incrementally (0°N, 36°N and 45°N). As the load increased, the crack propagated toward, and eventually passed, the three imaging locations as shown in Fig. 9 (the location of the crack tip is indicated by C_1, C_2, and C_3 at 0, 36, and 45 N respectively).

Figure 10 shows a series of images captured at position P_1 under the three successive loading states (0 N, 36 N and 45 N). In Fig. 10(a) (zero load), the mean tablet length is measured to be 8.8 µm, the mean tablet width is 0.45 µm and the mean organic layer thickness is 40 nm (shell B).

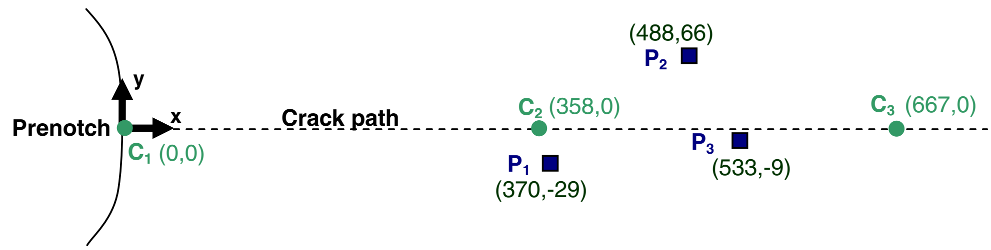

Fig. 9 Location of the three scanning positions (P_1, P_2 and P_3) in relation to the propagating crack in test #4. The location of the crack tip at three successive loads of 0, 36, and 45 N is indicated by C_1, C_2, and C_3 respectively. The coordinates of each position (x,y) are reported in units of microns relative to the origin located at the apex of the pre-notch

Figure 10(b) shows the same scanning regions after the first loading increment (36 N). At this time, the scanning region P_1 is located 29 μm below (corresponding to 3 rows of tablets) and 12 μm ahead of the crack tip. Though P_1 remains ahead of the crack at 36N, damage has spread to this region as is evident in the open gaps at the ends of the tables [a mean interface opening of 40 nm is measured in Fig. 10(b)].

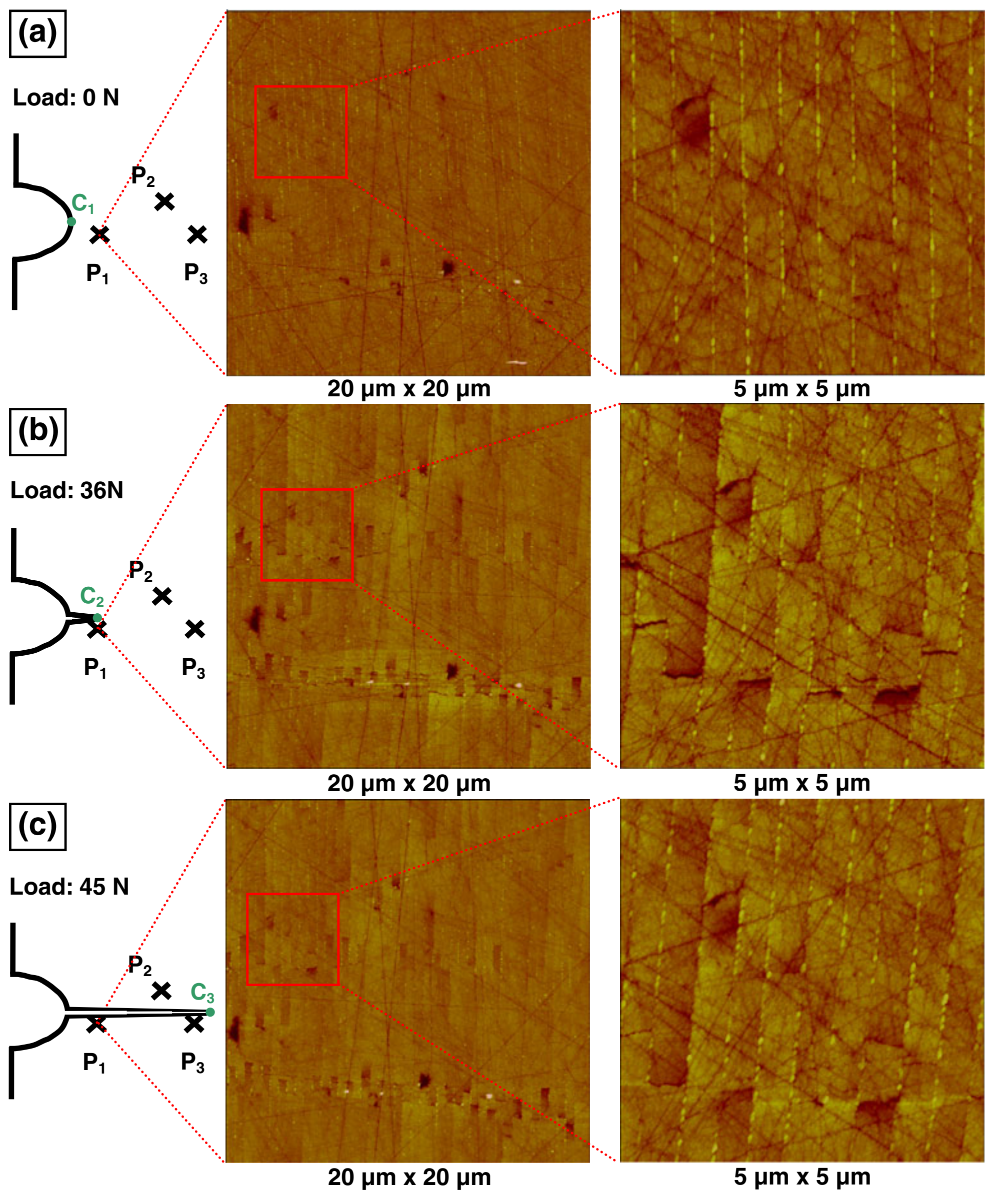

Fig. 10 AFM images (topography) acquired at position P_1 (see Fig. 9) at loads of 0 N, 36 N and 45 N, respectively

Figure 10(c) shows the region P_1 again after the second load increment (load: 45 N). P_1 is still located 29 μm below the crack path, but now is 297 μm behind the crack tip. Here, despite the increased load, the open gaps between tablets have actually closed partially. This partial relaxation in the wake of the crack is the result of the traction-free boundary introduced at the crack surface and has important implications in the material crack resistance as discussed in [9]. The relaxation in the wake region allows a re-arrangement of the tablets, prevents strain localization and premature failure, and is a key mechanism in what makes nacre so tough.

Figures 11 and 12 show a similar series of images at positions P_2 and P_3. Once again, as the load increases, the crack propagates, damage spreads and tablet interfaces open. However, tablet interface openings are minimal in the acquired images at position P_2. This is because P_2 is significantly further away from the crack (488 μm versus 29 μm or 9 μm as for P_1 or P_3 respectively, see Fig. 9), such that damage does not spread significantly to it. In contrast, tablet sliding and interfacial opening is prominent at point P_3, as in the case of P_1.

To quantify tablet sliding and its distribution, topographic AFM images were next post-processed using digital image correlation (DIC) techniques. The general framework of standard and discontinuous DIC is discussed next.

General Framework for Standard Digital Image Correlation

The framework of both standard and extended digital image correlation formulations used in this paper is based on

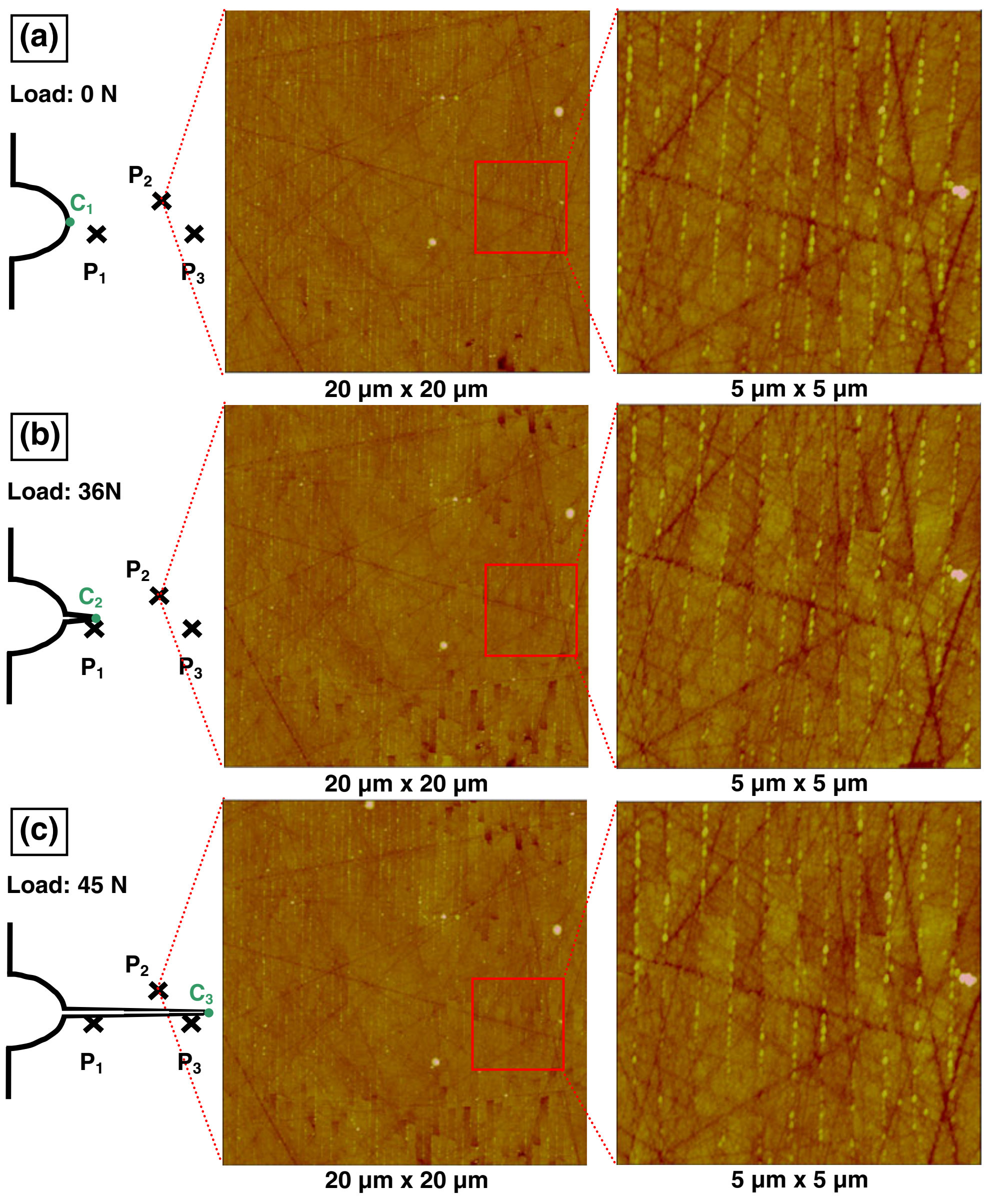

Fig. 11 AFM images (topography) acquired at position P_2 (see Fig. 9) at loads of 0 N, 36 N and 45 N, respectively

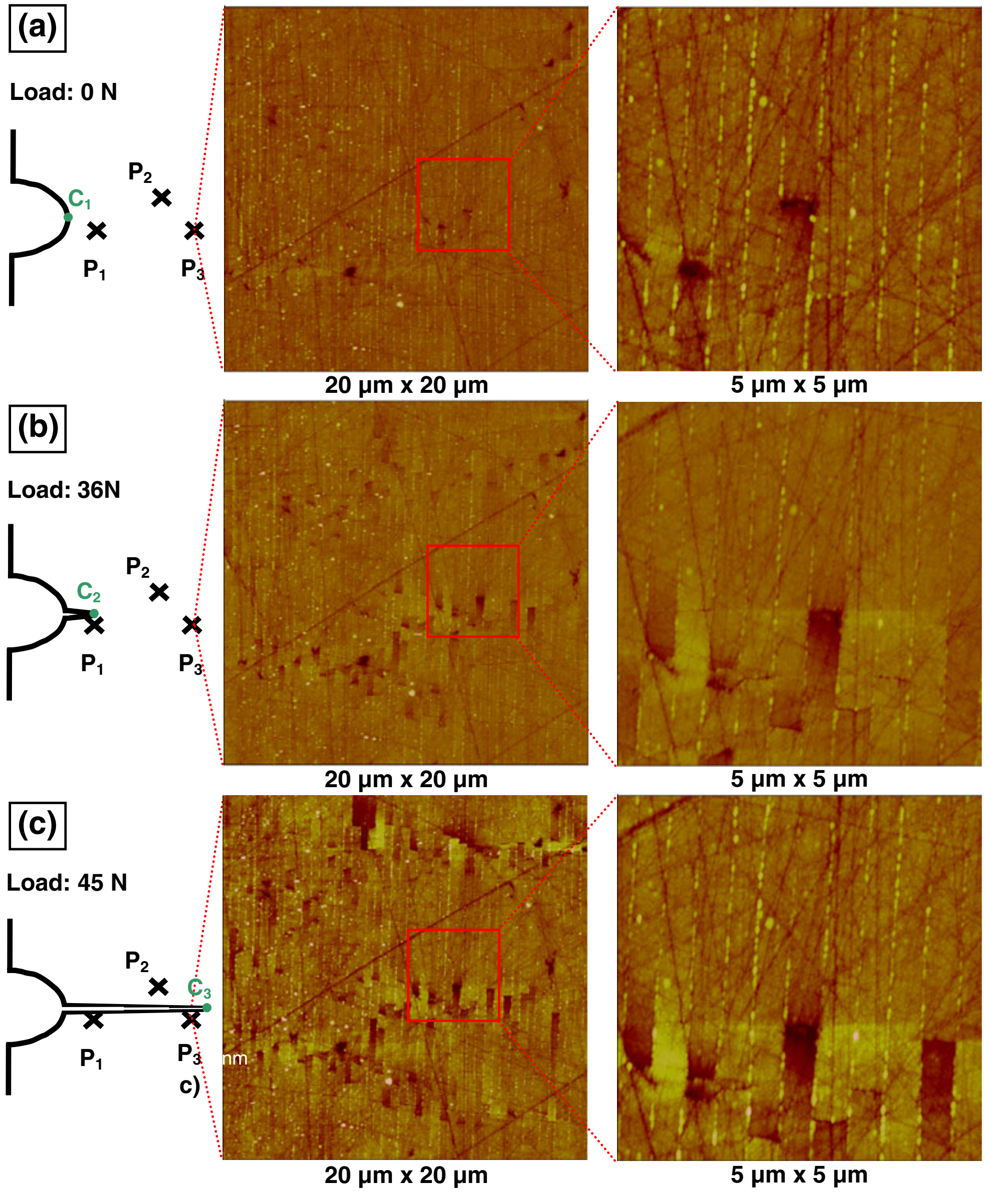

Fig. 12 AFM images (topography) acquired at position P_3 (see Fig. 9) at loads of 0 N, 36 N and 45 N, respectively

formulations presented by Grégoire et al. [24]. These are now applied to natural nacre and AFM image acquisition techniques reported herein.

The principle of DIC was advanced in the context of experimental mechanics by Sutton et al. [35, 36]. In DIC, two digital images corresponding to a reference and a deformed state are described by discrete functions representing the grey level of each pixel and related by

$$f^*(x^*) = f(x + d(x)) \quad (1)$$

where f and f^* are respectively the discrete functions of the reference and the deformed state, and $d(x)$ is the displacement field vector (Fig. 13).

The optimal displacement field determination consists of the minimization of a cross-correlation coefficient on a set of initial image pixels, called a subset:

$$C = 1 - \frac{\int_{\Delta M} f(x) f(x + d(x)) dx}{\sqrt{\int_{\Delta M} f^2(x) dx \int_{\Delta M} f^2(x + d(x)) dx}} \quad (2)$$

where ΔM is the surface of the subset in the reference image (see Fig. 14) and dx is a differential area.

The displacement field is typically decomposed on an appropriate functional basis on a subset:

$$d(P) = \sum_j n_j(P) u_j \quad (3)$$

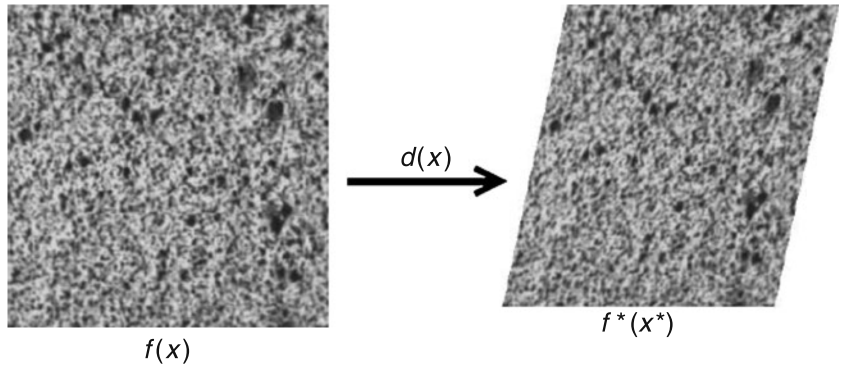

Fig. 13 Reference and deformed images

where u_j are the unknown displacement vectors, P is a point of the subset, $d(P)$ is its displacement vector given by the minimization of equation (2) and n_j are interpolating functions to be chosen.

According to the numbers of unknowns introduced in the decomposition, equation (3) is written as many times as needed to have a problem well-posed. Finally, the problem consists of inverting a matrix given by

$$D = [M]U \tag{4}$$

where D is the vector of the optimal displacements obtained by the minimization of equation (2), [M] is the matrix of the functional basis and U is the vector of the unknown displacements.

Typically, a bilinear continuous displacement field decomposition $(\{n_j\} = \{x, y, xy, 1\})$ and a cubic spline interpolation are used as in [37]. Figure 14 shows a subset before (ABCD centered on P) and after (A*B*C*D* centered on P*) deformation on the same coordinate system. The displacement field is estimated on each point by means of

$$\begin{cases} d_x(x,y) = u_1\widetilde{x} + u_2\widetilde{y} + u_3\widetilde{x}\widetilde{y} + u_4 \\ d_y(x,y) = u_5\widetilde{x} + u_6\widetilde{y} + u_7\widetilde{x}\widetilde{y} + u_8 \end{cases} \tag{5}$$

In the above equations, $\widetilde{x} = (x - x_A)/L$ and $\widetilde{y} = (y - y_A)/L$ are the homogeneous coordinates and L is the subset length. There are eight unknowns u_j so equations (5) are written at each point A, B, C and D. The solution is obtained by inverting the 8-dimensional matrix equation (4).

Finally, the algorithm is carried out on each subset of the initial image in order to obtain the full field displacement with a resolution of 1/10 of a pixel.

Standard DIC techniques are very efficient in obtaining the full-field displacement of a continuous body, even in large deformation modes. However, the method fails to resolve displacement fields in cases of material or geometric discontinuities as shown in [24]. Therefore, standard DIC techniques are not well-suited to quantify tablet sliding at the interfaces in nacre due to the discontinuities across tablet interfaces, unless other approximations are introduced. In order to bring out the limits of classical DIC techniques, the displacement field in the sliding direction was first estimated through a standard DIC tool (Icasoft [38]).

Since DIC techniques involve comparisons between sets of pixels of reference and deformed pictures, better results are obtained for small tablet interface openings. Indeed, when the tablet interface opens, black pixels are generated in the deformed picture and these pixels have no pairs in the reference picture. This new information is difficult to process in general, so the DIC technique is carried out here on images acquired in scanning position P_2 (Fig. 11) where the tablet interface openings remain quite small. Reference [Fig. 15(a)—unloaded, see also Fig. 11 and Appendix A] and deformed [Fig. 15(b)—loaded to 36 N, see also Fig. 11] images were converted to grey level (512×512 pixels) and then processed. Figure 15(c) shows the y-displacement field estimated with Icasoft. Since the y-direction is close to the loading direction (and the direction of tablet sliding), the y-displacement field becomes strongly discontinuous when tablet sliding occurs and gaps between tablets open. Within a given tablet, the y-displacement is well estimated. However, there is significant noise and degradation at the tablet interfaces where the tablet sliding leads to strong displacement discontinuities. To address this, we present next an extended DIC method.

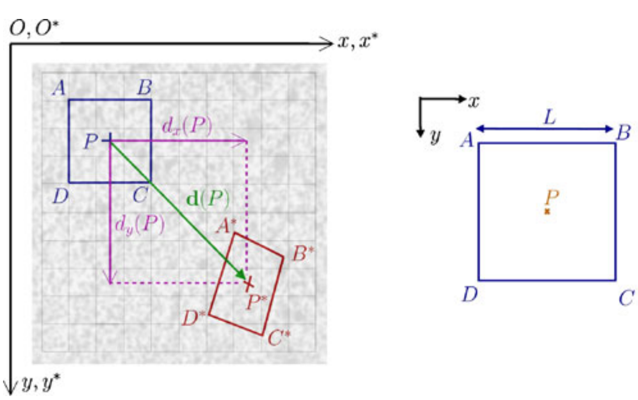

Fig. 14 Initial subset and deformed subset [24]

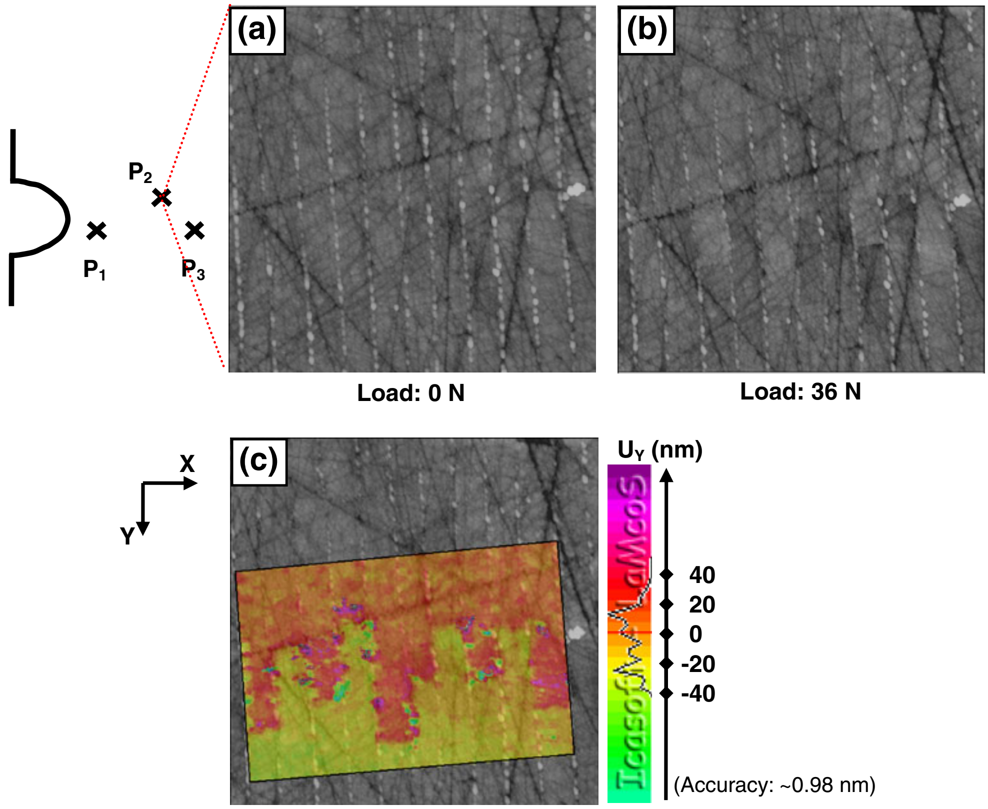

Fig. 15 Y-displacement field estimated with standard Icasoft DIC tool [38]. (**a**) Reference image (unloaded). (**b**) Deformed image (load: 36 N). (c) Y-displacement field

Before introducing the extended method, it is interesting to note that some of these limitations can be overcome through alternative methods of displacement field data analysis. Espinosa and coworkers [14] used a continuous DIC analysis to analyze relative sliding in nacre tablets from atomic force microscopy images. In their analysis, they compared the displacement profiles along the centerlines of adjacent tablets [white dashed lines in Fig. 16(d)]. In this region the displacements are relatively unaffected by discontinuities at the interfaces. Thus by taking the difference of the two displacement profiles and projecting them onto the interface [solid while/magenta line in Fig. 16(d)], they were able to determine the relative sliding along the interface [Δu_L in Fig. 16(g)]. Similarly, the transverse displacement field was obtained along a line perpendicular to the direction of tablet sliding [yellow line in Fig. 16(d)]. The results are shown in Fig. 16(h) as a function of load. Transverse dilation associated with tablet sliding is clearly observed. The implications of this result are discussed in Espinosa et al. [14].

General Framework for Extended Image Correlation

As explained in the previous section, standard digital image correlation formulations are based on the use of functional bases containing only continuous terms (equation (3) and (5)). In an analogy to the extended finite element method (XFEM) based on the partition of unity [39], discontinuous basis functions were proposed and applied to evolving discontinuities in dynamic crack localization [24] and direct fracture parameter estimation [40–42]. In these methods, the functional basis of the displacement field decomposition is enriched in order to take into account the geometrical discontinuity due to the presence of a crack.

Here we present the general framework of an extended image correlation technique based on the formulation proposed by Grégoire et al. [24, 40], but applied to quantify tablet sliding from AFM images acquired following the protocol discussed in the previous section. The bilinear continuous decomposition presented in equation (5) is preserved for smooth subsets (no interface) and when a subset is crossed by an interface (discontinuous subset) a discontinuous decomposition is employed, namely,

$$d(x) = \sum_j n_j(x)u_j = \begin{cases} \tilde{x}u_1 + \tilde{y}u_2 + \tilde{x}\tilde{y}u_3 + u_4(\text{smoothsubset}) \\ u_5 + F(x)u_6(\text{discontinuoussubset}) \end{cases} \quad (6)$$

$$\text{where } F(x) = \begin{cases} 1 \text{ if } x \text{ is above the interface} \\ 0 \text{ if } x \text{ is below the interface} \end{cases}$$

In the above equation, (u_j; $j\in[|1,6|]$) are unknown displacement vectors, $d(x)$ is given by the minimization of equation (2), $\tilde{x} = (x - x_A)/L$ and $\tilde{y} = (y - y_A)/L$ are the homogeneous coordinates on a subset and L is the subset

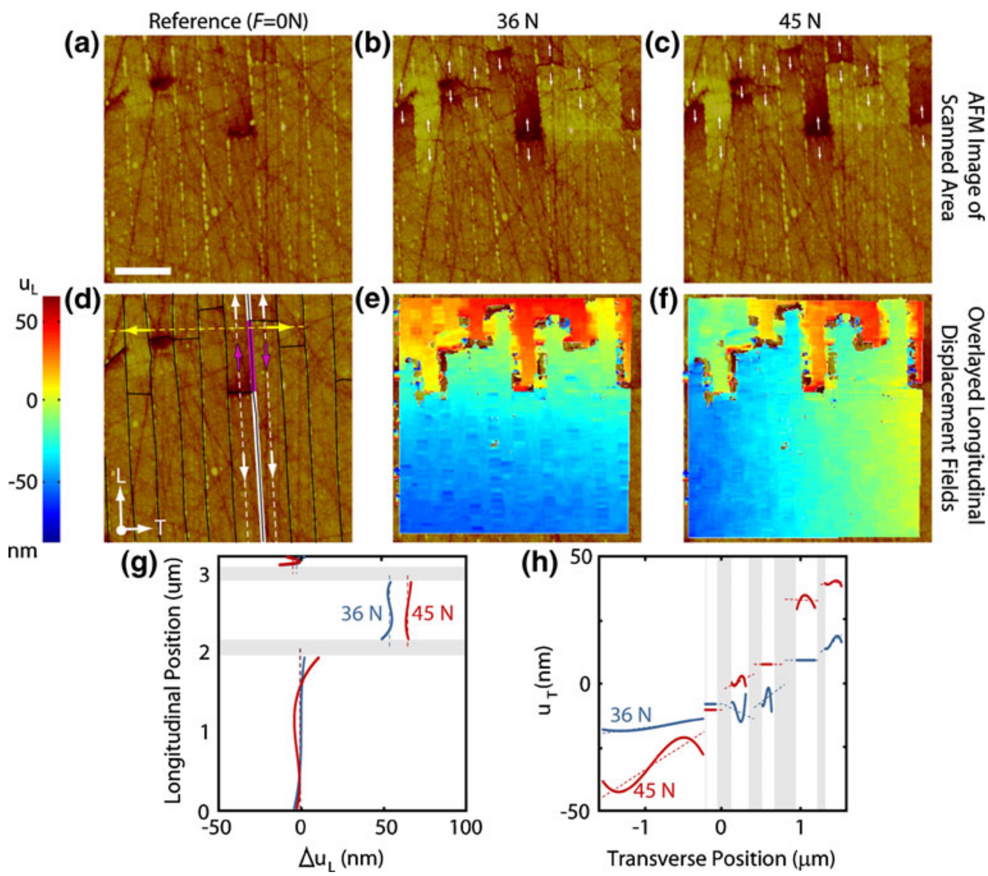

Fig. 16 Analysis of relative tablet displacements using alternative analysis of displacement field data (reproduced from [14]). (**a**–**c**) 5 μm×5 μm topographic AFM images at different loads. Height scale is 50 nm from black to white. (**d**) AFM image at zero load (same as (**a**)) showing the paths along which longitudinal (L) sliding (magenta) and transverse (T) dilation (yellow) were calculated. (**e**–**f**) Longitudinal displacement fields for images b and c with respect to image a. (**g**) Quantification of relative longitudinal tablet sliding in the overlap region (magenta in image **d**). (**h**) Quantification of transverse displacement where an overall transverse expansion is infered from the anaalysis (negative Poisson's effect)

length. For simplicity, the displacement field is only decomposed as a rigid body motion on a discontinuous subset but the terms corresponding to the elongations and the distortions may be enriched as well.

Equation (6) is written on each vertex of the subset. In case of a smooth subset, there are four unknown vectors and the solution consists of inverting an 8 by 8 matrix as in equation (4). In case of a discontinuous subset, there are only two unknown vectors and the solution consists of inverting an 8 by 4 matrix using its pseudo-inverse:

$$U = \begin{cases} [M]^{-1}D & \text{(smoothsubset)} \\ \left([M]^T[M]\right)^{-1}[M]^T D & \text{(discontinuoussubset)} \end{cases} \tag{7}$$

Finally, tangential and normal discontinuous jumps in the displacement are obtained at the interfaces. Here the tangential component corresponds to the sliding of neighboring tablets relative to each other. General tests of validation and performance of the proposed discontinuous decomposition are detailed in [24, 43]. In the discussion that follows, we will apply this technique to quantify tablet sliding in natural nacre.

Tablet Sliding Quantification and Its Distribution Along Interfaces

Figure 1(b) shows a schematic of typical tablet arrangements and the corresponding direction of tablet sliding under loading. For each tablet interface in Fig. 17(b), tablet sliding is calculated using the extended technique and its variation along the tablet interfaces plotted in Fig. 17. For each subset cut by an interface, the discontinuous decomposition (6) is applied and the tablet sliding, which corresponds to a jump in the tabgential displacement component, is estimated following:

$$\begin{aligned} [|u|] &= u^{above} - u^{below} = (u_5 + u_6) - u_5 \\ &= \underbrace{u_6.t}_{\text{tablet sliding}} \; t + (u_6.n)n \end{aligned} \tag{8}$$

where n and t are orthonormal and respectively normal and tangential to the discontinuity interface.

For clarity, images are rotated 90° counterclockwise in Fig. 17 and the interfaces between tablets highlighted in red. The overlap region in which relative sliding occurs [Fig. 1(b)] is marked by a dashed line. The tablet sliding is

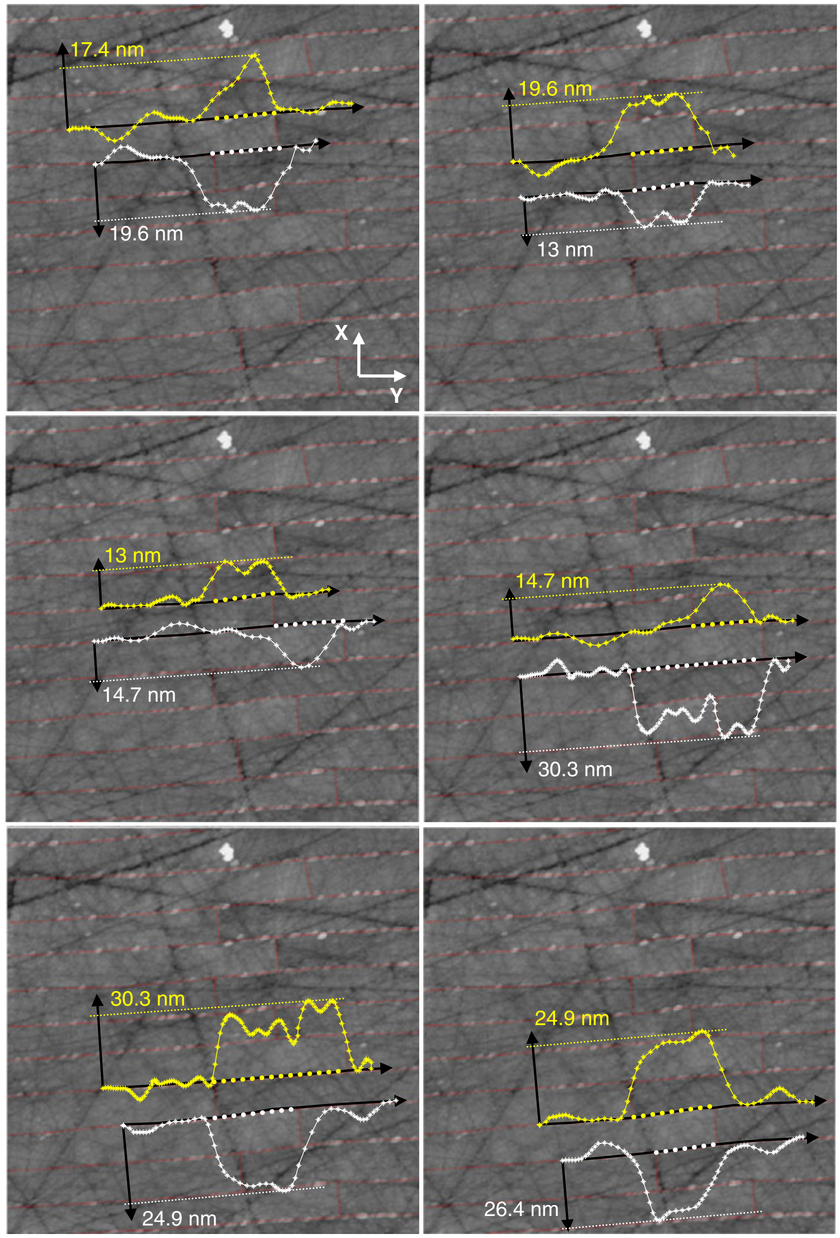

Fig. 17 Quantification of tablet sliding and its repartition along the tablet interfaces. Dotted line indicates the overlap region between neighboring tablets

plotted using the same scale at all interfaces. As expected, tablet sliding is always dominant in the overlap region, regardless of its magnitude. However, some sliding also appears in the core [i.e., out slide the overlap region, see Fig. 1(b)]. The majority of the time, this sliding in the core occurs in a direction opposite to that in the overalap region as previously predicted by numerical simulations [34]. Estimates of associated normal displacements (i.e., perpendicular to the direction of tablet sliding), as predicted by Espinosa and co-workers [9, 12, 34] proved beyond the present resolution of the current discontinuous DIC method. More algorithmic development or other approaches are needed to achieve such estimates.

Conclusion

This paper has shown how multiscale *in situ* experiments may lead to a better understanding of the fracture and damage mechanisms involved in the failure of materials with hierarchical microstructures. By applying extended digital image correlation and other image processing techniques, we can further extract *quantitative* information from these otherwise conventionally *qualitative* experiments. At the macroscale, the development and propagation of a white region was observed which is indicative of damage spreading around the main crack. At the microscale, this damage spreading was quantified using an iso-contour image processing technique and linked to the fracture resistance properties of nacre. Post-mortem scanning electron microscopy showed multiple interface openings widely spread from the crack indicative of the large white region seen at the microscale. At the nanoscale, a combination of well-controlled atomic force microscopy acquisition techniques and new algorithms based on digital image correlation provided quantification of tablet sliding and its distribution along the tablet interfaces. It was shown that tablet sliding is dominant in the overlap region between tablets, regardless of the magnitude of sliding, implying that tablet morphology plays a significant role in the fracture and damage mechanisms observed in nacre. The methodology described in this manuscript will enable the quantification of deformation mechanisms in biological and artificial materials (e.g., nanocomposites) with hierarchical structures through the ability to accommodate discontinuities that are present in the interfaces of such materials.

Acknowledgments HDE acknowledges the support by the National Science Foundation through award No. CMS-0301416, ARO-MURI Award No. W911NF-08-1-0541, ONR awards N00014-08-1-0108, N00014-08-1-1055, and General Motors Company through contract No. TCS10643. Carla Shute (Northwestern University) is gratefully acknowledged for her advice concerning the nacre sample preparation. D.G. is grateful to the French Ministry of Defense (DGA/D4S) for its support through grant No. 0860021 to visit Northwestern University as a research associate. O.L. acknowledges the Northwestern University Presidential and Ryan Fellowships.

Appendix A. Figures with Essential Color Discrimination

Certain figures in this article, particularly Figs. 6 and 15 are difficult to interpret in black and white. The full color images can be found in the on-line version.

References

1. Sarikaya M, Aksay IA (eds) (1995) Biomimetics, design and processing of materials. Woodbury, NY
2. Mayer G (2005) Rigid biological systems as models for synthetic composites. Science 310:1144
3. Buehler MJ, Ackbarow T (2007) Fracture mechanics of protein materials. Mater Today 10:46
4. Ashby MF, Gibson LJ, Wegst U, Olive R (1995) The mechanical properties of natural materials. I. Material property charts. Proc Math Phys Sci 450:123
5. Gao HJ, Ji BH, Jager IL, Arzt E, Fratzl P (2003) Materials become insensitive to flaws at nanoscale: lessons from nature. Proc Natl Acad Sci USA 100:5597
6. Currey JD (1977) Mechanical properties of Mother of Pearl in tension. Proc R Soc Lond 196:443
7. Currey JD, Taylor JD (1974) The mechanical behavior of some molluscan hard tissues. J Zool (London) 173:395
8. Wegst U, Ashby M (2004) The mechanical efficiency of natural materials. Philos Mag 84:2167
9. Barthelat F, Espinosa HD (2007) An experimental investigation of deformation and fracture of nacre-mother of pearl. Exp Mech 47:311
10. Lin A, Meyers MA (2005) Growth and structure in abalone shell. Mater Sci Eng A-Struct Mater Prop Microstruct Process 390:27
11. Su XW et al (2002) Structural and microstructural characterization of the growth lines and prismatic microarchitecture in red abalone shell and the microstructures of abalone “flat pearls”. Chem Mater 14:3106
12. Espinosa H, Rim J, Barthelat F, Buehler MJ (2009) Merger of structure and material in nacre and bone-perspectives on de novo biomimetic materials. Prog Mater Sci 54:1059
13. Launey M, Ritchie R (2009) On the fracture toughness of advanced materials. Adv Mater 21:2103–2110
14. Espinosa HD et al. (2011) Tablet-level origin of toughening in Abalone shells and translation to synthetic composite materials. Nature communications. doi:10.1038/ncomms1172
15. Wang RZ, Suo Z, Evans AG, Yao N, Aksay IA (2001) Deformation mechanisms in nacre. J Mater Res 16:2485
16. Ren F, Wan X, Ma Z, Su J (2009) Study on microstructure and thermodynamics of nacre in mussel shell. Mater Chem Phys 114:367
17. Meyers M, Lin A, Chen P, Muyco J (2008) Mechanical strength of abalone nacre: role of the soft organic layer. J Mech Behav Biomed Mater 1:76
18. Evans AG et al (2001) A model for the robust mechanical behavior of nacre. J Mater Res 16:2475
19. Song F, Bai YL (2003) Effects of nanostructures on the fracture strength of the interfaces in nacre. J Mater Res 18:1741
20. Smith BL et al (1999) Molecular mechanistic origin of the toughness of natural adhesives, fibres and composites. Nature (London) 399:761
21. Barthelat F, Li CM, Comi C, Espinosa HD (2006) Mechanical properties of nacre constituents and their impact on mechanical performance. J Mater Res 21:1977
22. Li XD, Huang Z (2009) Unveiling the formation mechanism of pseudo-single-crystal aragonite platelets in nacre. Phys Rev Lett 102:1
23. Bruet BJF et al (2005) Nanoscale morphology and indentation of individual nacre tablets from the gastropod mollusc Trochus niloticus. J Mater Res 20:2400
24. Grégoire D, Maigre H, Morestin F (2009) New experimental techniques for dynamic crack localization. Eur J Comput Mech 18:255
25. Clegg WJ, Kendall K, Alford NM, Button TW, Birchall JD (1990) A simple way to make tough ceramics. Nature 347:455
26. Mayer G (2006) New classes of tough composite materials: lessons from natural rigid biological systems. Mater Sci Eng C Biomim Supramolec Syst 26:1261
27. Tang ZY, Kotov NA, Magonov S, Ozturk B (2003) Nano-structured artificial nacre. Nat Mater 2:413
28. Podsiadlo P et al (2007) Ultrastrong and stiff layered polymer nanocomposites. Science 318:80
29. Bonderer LJ, Studart A, Gauckler L (2008) Bioinspired design and assembly of platelet reinforced polymer films. Science 319:1069
30. Chen L, Ballarini R, Kahn H, Heuer AH (2007) A bioinspired micro-composite structure. J Mater Res 22:124
31. Zhang X, Liu C, Wu W, Wang J (2006) Evaporation-induced self-assembly of organic–inorganic ordered nanocomposite thin films that mimic nacre. Mater Lett 60:2086
32. Munch E et al (2008) Tough, bio-inspired hybrid materials. Science 322:1516

33. A. S. T. M. Standard E1820-01 (2001) Standard test method for measurement of fracture toughness. ASTM International
34. Barthelat F, Tang H, Zavattieri PD, Li CM, Espinosa HD (2007) On the mechanics of mother-of-pearl: a key feature in the material hierarchical structure. J Mech Phys Solids 55:306
35. Sutton MA, Cheng MQ, Peters WH, Chao YJ, Mcneill SR (1986) Application of an optimized digital correlation method to planar deformation analysis. Image Vis Comput 4:143
36. Sutton MA, Wolters W, Peters WH, Ranson W, Mcneill SR (1983) Determination of displacements using an improved digital correlation method. Image Vis Comput 1:133
37. Touchal-Mguil S (1997) (In French) Une technique de corrélation d'images numériques: application à la détermination de courbes limites de formages et proposition d'un critère de striction. INSA-LYON, France
38. http://icasoft.insa-lyon.fr, Icasoft, Morestin in LaMCoS, INSA-Lyon.
39. Moes N, Dolbow J, Belytschko T (1999) A finite element method for crack growth without remeshing. Int J Numer Methods Eng 46:131
40. Gregoire D, Maigre H, Combescure A (2009) New experimental and numerical technique to study the arrest and the restart of a crack under impact in transparent materials. Int J Solids Struct 46:3480
41. Poissant J, Barthelat F (2010) A novel “subset splitting” procedure for digital image correlation on discontinuous displacement fields. Exp Mech 50:353
42. Réthoré J, Hild F, Roux S (2008) Extended digital image correlation with crack shape optimization. Int J Numer Methods Eng 73:248
43. Grégoire D, Maigre H, Fabis J, Combescure A (to be submitted, 2010) New experimental techniques for crack location and fracture parameters estimation in non-transparent materials. Exp Mech